Dalton Transactions

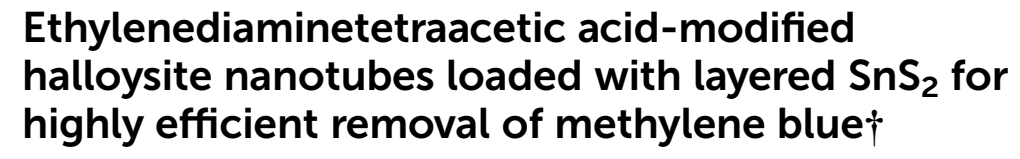


PAPER

View Article Online
View Journal | View Issue



Cite this: *Dalton Trans.*, 2025, **54**, 12201



Lan Yang, Qiyuan Lu, Xiao Zhou, Tao Yang and Chunfang Du 0 *

Adsorption is an effective strategy for treating water pollution and natural clay mineral-based materials exhibit great potential for removing pollutants from wastewater. In this paper, halloysite nanotubes (HNTs) modified with ethylenediaminetetraacetic acid (EDTA) were thermally treated to serve as supports for loading SnS_2 to construct $SnS_2/HNTs(C)$ (SHC_x-y). Methylene blue (MB) was selected as a target pollutant to examine the removal efficiency of the obtained adsorbents. $SHC_{0.04}$ -500 could remove more than 90% of MB (50 mg L⁻¹) within 18 min, which was 9 and 18 times higher than those of SnS_2 and HNTs(C)-500, respectively. Moreover, the adsorbent $SHC_{0.04}$ -500 with good pH and temperature adaptability exhibited excellent adsorption performance toward cationic dyes and various antibiotics. The adsorption process of MB over $SHC_{0.04}$ -500 matched well with the Langmuir isotherm and the pseudo-first-order kinetic model. The adsorption mechanism investigation suggested that the carbon layer on HNTs made the surface of $SHC_{0.04}$ -500 more negative, which mostly contributed to the improved adsorption performance. This work provides a low-cost, environmentally friendly, and efficient adsorbent for removing pollutants from wastewater and contributes a new strategy to enhance the removal efficiency by a simple modification method.

Received 14th June 2025, Accepted 12th July 2025 DOI: 10.1039/d5dt01400j

rsc.li/dalton

Introduction

With the rapid development of modern industry, a large number of pollutants from textile, paint, leather, and other industries are discharged into water systems, which bring serious effects to the ecological environment and human health.^{1–6} Therefore, it is urgent to find more efficient, economical, and environmentally friendly methods to remove pollutants from water.

At present, there are multiple available techniques for treating water pollutants, including photocatalytic degradation, Fenton reaction, adsorption and so on. The degradation process refers to the breaking of a large organic dye structure into small molecules, which may produce toxic or harmful chemicals if the degradation is insufficient.^{7–10} Compared to degradation, adsorption has received much attention because of its simplicity, low cost, safety, and non-toxicity.¹¹ A large number of adsorbents such as biochar, graphene oxide, and MOF composites have been applied in the removal of organic

College of Chemistry and Chemical Engineering, Inner Mongolia University, Hohhot, Inner Mongolia, 010021, P. R. China. E-mail: cedchf@imu.edu.cn;

Fax: +86-471-4994375: Tel: +86-471-4994375

†Electronic supplementary information (ESI) available. See DOI: https://doi.org/ 10.1039/d5dt01400j

pollutants. 12-14 However, the specific surface area and porosity of the above adsorbents are generally affected by the raw materials and preparation conditions, leading to an uncontrollable adsorption efficiency. 15 Natural clay minerals have the advantages of large specific surface area, stable structure, and easy modification. It has been reported that the combination of minerals and adsorbents can overcome the shortcomings mentioned above and be a potential strategy for water pollution treatment.16,17 Halloysite nanotubes (HNTs) are composed of curled silicate layers with a hollow tubular morphology.18 The inner and outer walls of HNTs are composed of alumina octahedra and silica-oxygen tetrahedra, respectively, both of which contain a certain number of hydroxyl groups. 19 This structural characteristic indicates that the chemical modification of HNTs could be easily achieved. Moreover, HNTs have a rich porous structure, a large specific surface area, a high aspect ratio, and low cost.^{20,21} In recent years, the application of HNTs in water treatment has been further explored. For instance, HNTs modified with (3-aminopropyl) triethoxysilane (H-APTES) exhibited excellent removal efficiencies toward both Cu²⁺ ions and reactive red 120 azo dye (RR-120).²² A MgAl-LDH/HNT composite showed a highly efficient CO2 adsorption performance with an adsorption capacity of 3.91 mmol g^{-1} .²³ Thus, HNTs could be a potential and ideal material to construct functional mineral composites for removing water pollutants.24,25

Paper **Dalton Transactions**

Recently, SnS₂ has received increasing attention in water treatment due to its good adsorption performance, stable chemical properties, and simple synthesis.26-28 SnS2 nanoparticles exhibited an adsorption efficiency of 85% toward rhodamine B within 180 min.²⁹ Compared to SnS₂ with other morphologies, layered SnS₂ could remove a large number of toxic organic dyes by selective adsorption, which further highlighted its advantages in pollutant removal.³⁰ Moreover, the layered structure could effectively improve the diffusion of dye molecules, provide better transport paths, and offer a large number of adsorption sites for the adsorption process.

It was reported that the carbon modification of HNTs could bring about an expansion of the specific surface area and an increase in the number of adsorption sites, which further improved the adsorption efficiency.31 Thus, it is anticipated that composites constructed using HNTs with carbon modification and layered SnS2 could be ideal and potential adsorbents for removing water pollutants. 32,33

In this work, HNTs modified with EDTA after calcination were used as supports for loading layered SnS2 to construct $SnS_2/HNTs(C)$ (SHC_x-y) composites. The synthesized adsorbents possessed large specific surface areas, rich porous structure, and more negative surface charge, making them suitable for MB removal. The adsorption conditions including MB concentration, adsorbent dosage, temperature, and pH value were systematically optimized. The important role of carbon modification of HNTs in enhancing the removal efficiency was emphatically discussed. Moreover, the adsorption process of MB over SHC_{0.04}-500 was examined and a plausible adsorption mechanism was put forward.

Experimental

Materials and methods

Halloysite nanotubes (HNTs) were purchased from Guangzhou Runwo Material Technology Co. Ltd. Ethylenediaminetetraacetic acid (EDTA) was purchased from Tianjin Xinbute Chemical Co. Tin chloride pentahydrate (SnCl₄·5H₂O) was purchased from Tianjin Beilian Fine Chemicals Development Co. Methylene blue (MB) was purchased from Beijing Inokai Technology Co. Thiourea (CH₄N₂S), sodium hydroxide (NaOH), hydrochloric acid (HCl), and absolute ethanol (EtOH) were purchased from Tianjin Fengchuan Chemical Reagent Technology Co. Malachite green (MG), methyl violet (MV), orange yellow (OA), and methyl orange (MO) were purchased from Aladdin Ltd. Norfloxacin (NFO), ofloxacin (OFX), and tetracycline hydrochloride (TC) were purchased from Shanghai Meryer Chemical Reagent Co. All reagents were used without further purification. The crystal structures of the samples were examined by X-ray diffraction (XRD, Empyrean Panalytical, Netherlands). The size and morphology of the samples were determined by scanning electron microscopy (SEM, HITACHI S-4800, Japan). Transmission electron microscopy (TEM) was performed using a Talos F200S G2 instrument. X-ray photoelectron spectroscopy (XPS) was performed using a Thermo Fisher K-alpha instrument, recording the surface elemental compositions and their chemical states. The changes of molecular structure were studied by Fourier transform infrared spectroscopy (FT-IR, VERTEX70). The zeta potentials at different pH values were obtained using a Malvern Zetasizer Nano ZS90 instrument. The specific surface areas of the samples were obtained using the Brunner-Emmett-Teller method (BET, Quantachrome, USA). Raman spectra were recorded using a Horiba Scientific LabRAM HR Evolution spectrometer with an excitation wavelength of 325 nm over the range of 1000-2000 cm⁻¹.

Pretreatment of HNTs

HNTs (2.5 g) were dispersed in deionized water (150 mL) under ultrasonic treatment for 30 min. EDTA (7.5 g) was dissolved in the above solution and kept at 80 °C for 24 h. Subsequently, the solid was centrifuged, washed with deionized water and ethanol several times, and dried at 60 °C overnight. The powders were calcined under an air atmosphere at different temperatures for 3 h (6 °C min⁻¹) in a muffle furnace. The obtained products were named HNTs(C)-y (y indicates the calcination temperature for HNTs, y = 400, 500, 600,and 800 °C).

Synthesis of SHC_r-v

A series of SnS₂/HNTs(C) samples were synthesized by a onepot hydrothermal method. In a typical synthesis process, different amounts of HNTs(C)-500, 0.14 g of SnCl₄·5H₂O, and 3.12 g of thiourea were dispersed and dissolved in 35 mL of deionized water with stirring for 30 min. The mixture was kept at 180 °C for 18 h in a Teflon reactor. The samples were cooled to room temperature and washed with deionized water and ethanol alternately several times and dried at 60 °C overnight. The obtained products were named SHC_x -500 (x indicates the different amounts of HNTs(C)-500, x = 0.04, 0.1, 0.3, and 0.5 g). For comparison, pure SnS2 was also prepared by using the same synthesis method as the composites just without the addition of HNTs(C)-500.

Adsorption experiment

In a typical adsorption experiment, 20 mg of $SHC_{0.04}$ -500 was dispersed in 20 mL of MB (50 mg L⁻¹) solution at room temperature. A certain amount of the suspension was removed and filtered at 3 min intervals. The concentration of MB was analyzed by UV-Vis spectroscopy. The adsorption efficiency (%) and adsorption capacity (q_e) were calculated from eqn (1) and (2), respectively:

Adsorption efficiency (100%) =
$$\frac{(C_0 - C_t)}{C_0}$$
 (1)

$$q_{\rm e} = \frac{(C_0 - C_{\rm e})V}{M} \tag{2}$$

where C_0 is the initial concentration of MB, q_e is the adsorption capacity, V is the volume of MB, and M is the mass of the adsorbent. C_t and C_e are the concentrations at moment t and at adsorption equilibrium, respectively.

In order to investigate the wide applicability of the adsorbent, various organic dyes (MV, OA, and MO) and antibiotics

Dalton Transactions Paper

(OFX, NFO, and TC) were selected to conduct adsorption tests. The concentrations of the above pollutant solutions were all 50 mg L^{-1} .

Recycling experiment

The SHC_{0.04}-500 sample after the adsorption experiment was dispersed in anhydrous methanol and stirred for 24 h. After centrifugation, it was dried overnight in an oven at 60 $^{\circ}$ C and then reused in the subsequent adsorption experiments.

Results and discussion

Synthesis and structural characterization

In order to analyze the morphology and structure of pure and composite samples, SEM and TEM techniques were adopted. As shown in Fig. 1a, pure HNTs have a tube structure with a length of approximately 1–2 μ m and a diameter of 50–100 nm. The modified HNTs maintained the tubular morphology and smooth surface of pure HNTs, suggesting that calcination at 500 °C had little effect on the tubular morphology of HNTs (Fig. 1b). As shown in Fig. 1c, SnS₂ was stacked by smooth hexagonal-like nanosheets with a diameter ranging from 50 to 500 nm. The SEM image of SHC_{0.04}-500 (Fig. 1d) demonstrated that SnS₂ nanosheets come in close contact with HNTs(C)-500 nanotubes, enhancing the dispersion of SnS₂ in the composite and thereby more active sites could be exposed.

Fig. 2a shows the TEM image of $SHC_{0.04}$ -500. It could be clearly observed that SnS_2 nanosheets were uniformly anchored on the surface of HNTs(C)-500, demonstrating the successful synthesis of $SHC_{0.04}$ -500. The red area in the HRTEM image signifies the amorphous graphite carbon, indicating the anticipated carbon modification of HNTs (Fig. 2b). Additionally, the lattice spacing of 0.27 nm was indexed to the (101) crystal plane of SnS_2 , verifying the well-crystallized structure of SnS_2 in the composite. In Fig. 2c, carbon was found to be uniformly distributed across the entire structure, further confirming the successful carbon modification of HNTs. Notably, Al and Si elements were detected in the tubular

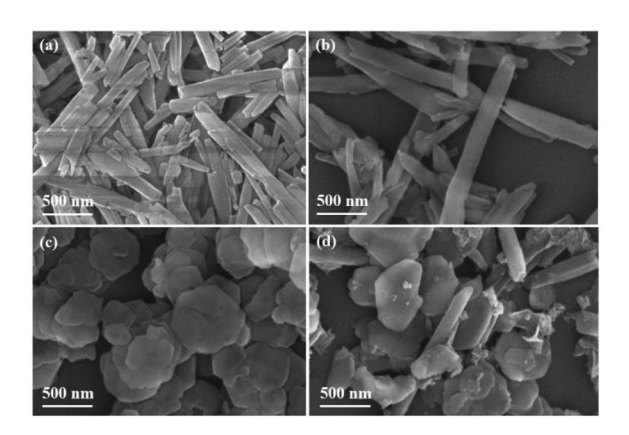


Fig. 1 SEM images of HNTs (a), HNTs(C)-500 (b), SnS_2 (c), and $SHC_{0.04}$ -500 (d).

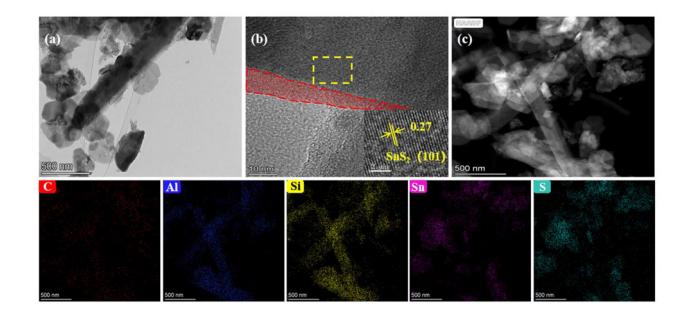


Fig. 2 TEM (a), HRTEM (b), and TEM elemental mapping images (c) of $SHC_{0.04}$ -500.

regions, while Sn and S elements were concentrated in the hexagonal lamellar domains. This spatially correlated elemental distribution provided direct evidence for the intimate integration of HNTs(C)-500 and SnS_2 , further confirming the successful synthesis of the $SHC_{0.04}$ -500 composite.

To further elucidate the detailed structural information and compositions of all samples, XRD and FT-IR techniques were adopted. The XRD patterns of HNTs and pure SnS_2 matched well with the standard PDF cards of HNTs and SnS_2 (JCPDS No. 09-0453 and JCPDS No. 23-0677), respectively (Fig. 3a). The characteristic peaks located at 15.0° , 32.1° , and 41.9° correspond to the (001), (101), and (102) crystal planes of SnS_2 , respectively. The broad peak at 24° in the XRD pattern of HNTs(C)-500 indicates the presence of amorphous carbon. The carbon layer might make it difficult to detect the characteristic peaks of HNTs. Therefore, $SHC_{0.04}$ -500 obviously showed the diffraction peaks of SnS_2 , and the intensity of the SnS_2 diffraction peaks increased with a decrease in the addition amount of HNTs(C)-500 (Fig. $S1^{\dagger}$).

The FT-IR spectra of the pure and composite samples are shown in Fig. 3b. The absorption peaks at 542 and 912 cm⁻¹ in HNTs belong to the bending vibration of Al-O-Si and the deformation vibration of Al-OH, respectively.³⁷ The absorption

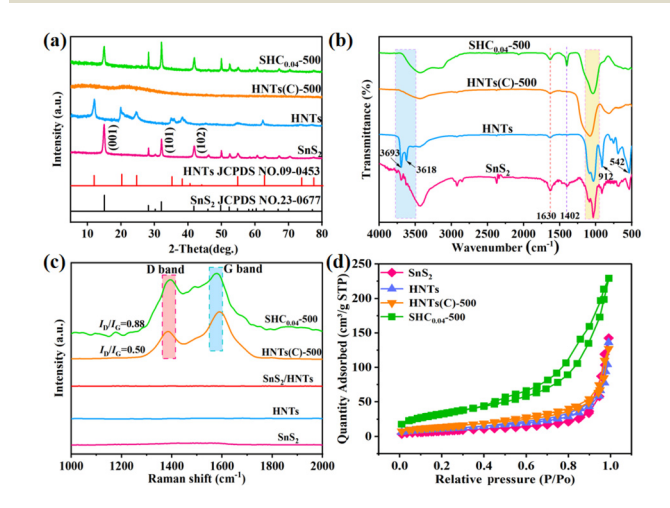


Fig. 3 XRD patterns (a), FT-IR spectra (b), Raman spectra (c), and N_2 adsorption—desorption isotherms (d) of various samples.

Paper Dalton Transactions

peaks at 1022 and 1107 cm⁻¹ correspond to the stretching vibrations of Si-O-Si and Si-O bonds in HNTs, respectively. In the spectrum of SnS₂, the characteristic peak at 1402 cm⁻¹ was attributed to the vibration of Sn-S bonds.38 For SnS2 and HNTs, the absorption peaks at 3618 and 3693 cm⁻¹ were attributed to the stretching vibrations of the hydroxyl groups on the surfaces of SnS₂ and HNTs, respectively. 16 Notably, the two broad peaks near 1100 and 3600 cm⁻¹ disappeared after HNT modification, indicating that the hydroxyl groups were removed from the surfaces of HNTs after high-temperature calcination.³⁹ All samples showed the peak at 1630 cm⁻¹, which was attributed to the adsorbed water molecules. It was noteworthy that the peak at around 1000 cm⁻¹ in SHC_{0.04}-500 shifted compared with that in pure HNTs(C)-500, which might be caused by the formation of new Si-O-Sn bonds. 40 The above phenomenon proved the successful combination of SnS₂ with HNTs(C)-500. 41 The intensity of the peak at 1402 cm⁻¹ in SHC_{0.04}-500 increased in contrast to that of SnS₂, which might be due to that there was a strong interaction between the C-C bond in HNTs(C)-500 with the Sn-S bond in SnS₂. 40

Raman spectrometry was employed to confirm the graphitization of various samples (Fig. 3c). There were two significant bands at 1385 and 1590 cm $^{-1}$ in SHC_{0.04}-500 and HNTs(C)-500, which imply the point defect degree (D band) and the graphitic structures (G band), respectively. The intensity ratio of the D band to the G band ($I_{\rm D}/I_{\rm G}$) is generally used to describe the degree of graphitization of samples. The larger the ratio, the greater the degree of graphitization, *i.e.*, more defects were produced. According to the Raman results, the $I_{\rm D}/I_{\rm G}$ value of SHC_{0.04}-500 (0.88) was significantly higher than that of SnS₂/HNTs (0), suggesting that the modification of HNTs with EDTA and subsequent calcination positively affected the graphitization of SHC_{0.04}-500. 42 The D and G bands were not observed in pure SnS₂ and HNTs.

Fig. 3d shows the N_2 adsorption–desorption isotherms of various samples. All the prepared samples exhibited type IV isotherms. SHC_{0.04}-500 had an obvious hysteresis loop, which was characteristic of a mesoporous structure. The SHC_{0.04}-500 sample exhibited the largest specific surface area (118.49 m² g⁻¹), which was larger than those of SnS₂ (30.90 m² g⁻¹), HNTs (40.09 m² g⁻¹), and HNTs(C)-500 (52.24 m² g⁻¹). The larger specific surface area of SHC_{0.04}-500 endowed it with more adsorption sites, which was favorable for enhancing the adsorption efficiency of SHC_{0.04}-500.

Fig. 4 shows the survey XPS spectra of SnS_2 , HNTs, HNTs (C)-500, and $SHC_{0.04}$ -500 as well as the high-resolution XPS spectra of each element. Fig. 4a shows that Sn, S, O, Si, Al, and C elements were all present in the $SHC_{0.04}$ -500 sample. The high-resolution C 1s spectra are shown in Fig. 4b. The characteristic peaks appearing at 288.9, 286.5, and 284.8 eV were attributed to the O-C=O, C-O, and C-C bonds, respectively. The peak area of sp² hybridized carbon (284.8 eV) increased from 60.48% (HNTs) to 73.64% (HNTs(C)-500), indicating that modification of HNTs with EDTA was beneficial for increasing the graphitic carbon content, which was consistent with the results of Raman analysis. The content of C-C in $SHC_{0.04}$ -500

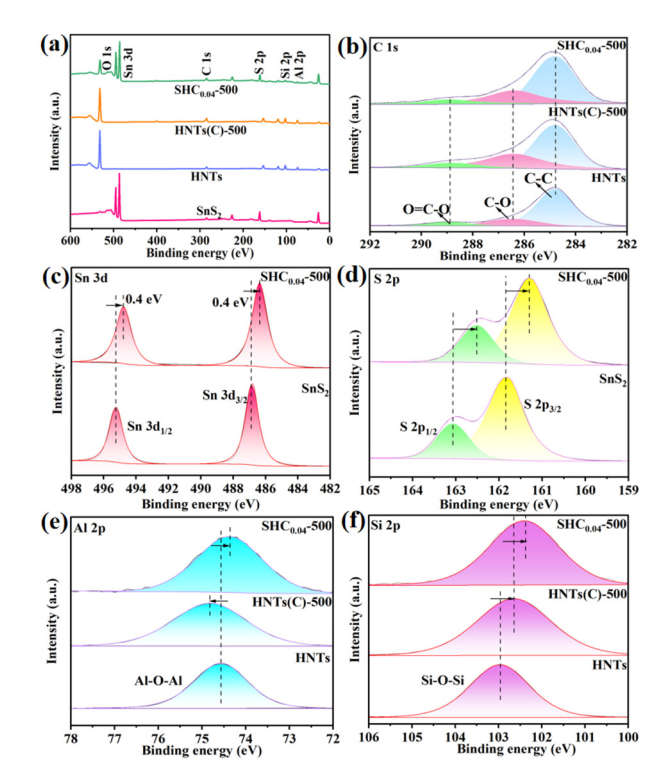


Fig. 4 Survey XPS spectra (a) and high-resolution spectra of C 1s (b), Sn 3d (c), S 2p (d), Al 2p (e), and Si 2p (f) of various samples.

was 70.6%, which was slightly smaller than that of C–C in HNTs(C)-500. This phenomenon suggested that some of C–C bonds in HNTs(C)-500 were broken and reorganized due to the interaction between $\rm SnS_2$ and $\rm HNTs(C)$ -500 during the synthesis process. ⁴⁴

As shown in Fig. 4c, Sn 3d spectra exhibited two binding energies at 494.8 and 486.4 eV, belonging to Sn $3d_{1/2}$ and Sn $3d_{3/2}$, respectively. In comparison with pure SnS₂, the fitted peak of Sn 3d in SHC_{0.04}-500 shifted to a lower-binding-energy position. In Fig. 4d, the characteristic peaks attributed to S $2p_{3/2}$ and S $2p_{1/2}$ orbitals shifted from 163.1 and 161.8 eV in SnS₂ to 162.5 and 161.3 eV in SHC_{0.04}-500, respectively, which suggested that the presence of HNTs(C)-500 had an effect on the electronic state of SnS₂. 45,46

Fig. 4e and f separately show the characteristic peaks of Al 2p and Si 2p. For HNTs, both Al-O-Al and Si-O-Si bonds showed only one characteristic peak at 74.3 and 102.4 eV, respectively. In comparison with HNTs, the peak positions of Al 2p and Si 2p in SHC_{0.04}-500 shifted to a lower binding-energy position. It was noteworthy that the binding energies of Sn 3d, S 2p, Al 2p, and Si 2p in SHC_{0.04}-500 were all lower than those of pure SnS₂ and HNTs(C)-500. This phenomenon not only confirmed the successful preparation of SHC_{0.04}-500 but also provided direct evidence that SnS₂ and HNTs(C)-500 were not merely physically mixed. Instead, their intrinsic electronic environments had been modified through interfacial interactions, which altered the electron distribution around these elements and thereby resulted in the observed decrease in binding energy.⁴⁷

Dalton Transactions Paper

MB was selected as the target pollutant to investigate the removal performance of various samples. The SnS₂, HNTs, and HNTs(C)-500 samples could adsorb a small amount of MB with adsorption efficiencies of only 10.5%, 9.1%, and 5.0% within 18 min, respectively (Fig. 5a). The adsorption efficiency of SHC_{0.04}-500 was significantly improved, showing about 90% adsorption efficiency toward MB within 18 min, which was about 9, 10, and 18 times as those of SnS2, HNTs, and HNTs (C)-500, respectively.

For exploring the optimal calcination temperature of modified HNTs, adsorption tests of MB over a series of SHC_{0.5}-y samples were performed. As shown in Fig. 5b, it could be observed that the adsorption efficiencies of the composites increased first and then decreased with increasing the calcination temperature of HNTs(C). At a lower temperature of 400 °C, the graphitization of the HNTs(C)-400 was low, which was not favorable for adsorption. When the calcination temperature reached 500 °C, the carbon in HNTs(C) formed a more regular graphite structure, resulting in a stronger interaction between the carbon layer and MB molecules, which could significantly improve the adsorption capacity.⁴⁸ However, with further increasing the temperature, the adsorption sites decreased due to the oxidation of the carbon layer on HNTs. 49 Based on the above analysis, 500 °C was adopted as the optimal calcination temperature in the following experiments.

Fig. 5c shows the effect of HNTs(C)-500 dosage on the adsorption efficiency of SHC_x-500. The adsorption efficiency increased first and then decreased with an increase of HNTs (C)-500 dosage. Based on the economic consideration, 0.04 g was selected as the optimal HNTs(C)-500 dosage in the subsequent experiments.

Fig. 6a shows the influence of MB concentration on the adsorption performance of SHC_{0.04}-500. The adsorption efficiency could reach more than 90% within 18 min, which decreased gradually with further increasing the initial MB concentration. The decreased adsorption efficiency indicated the insufficient active sites of SHC_{0.04}-500 for the enhanced number of MB molecules. Therefore, the initial MB concentration of 50 mg L⁻¹ was chosen for the next experiments. Fig. 6b shows the effect of $SHC_{0.04}$ -500 dosage (5, 10, 15, 20, 25, and 30 mg) on the removal efficiency of MB. The adsorption efficiency increased obviously with an increase of SHC_{0.04}-500 dosage and reached 100% when the SHC_{0.04}-500 dosage was enhanced to 25 mg, which remain unchanged with further increasing the adsorbent dosage to 30 mg. This phenomenon might be explained by the increased number of active sites

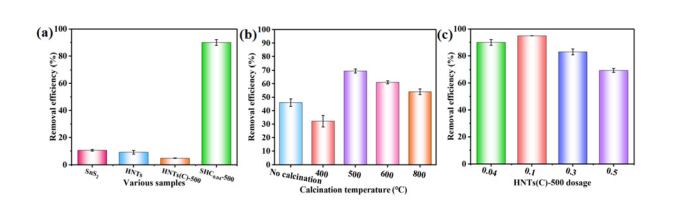


Fig. 5 The adsorption efficiencies of various samples (a), HNTs(C) at different calcination temperatures (b), and HNTs(C)-500 with different dosages toward MB (c).

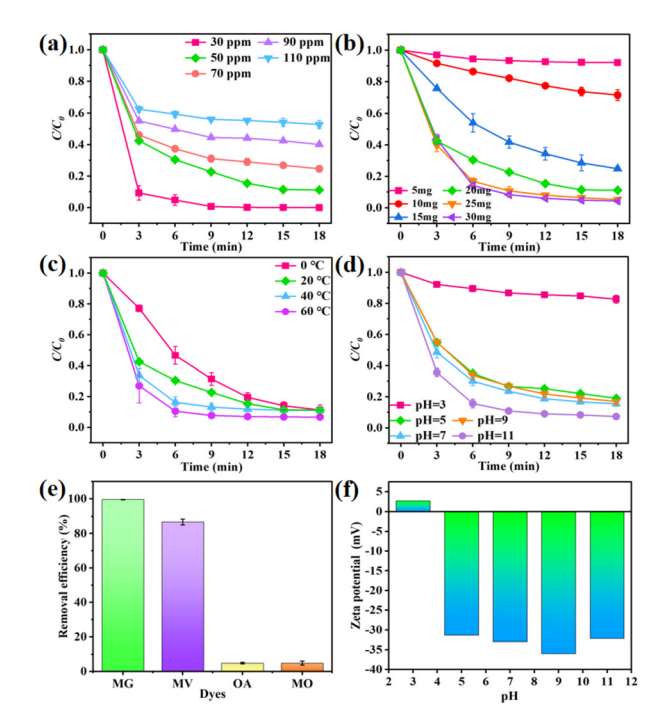


Fig. 6 Effects of MB concentration (a), adsorbent dosage (b), temperature (c), and pH value (d) on the adsorption efficiency of $SHC_{0.04}$ -500. The adsorption efficiencies of SHC_{0.04}-500 toward various dyes (e). Effect of the pH value on the zeta potential of SHC_{0.04}-500 (f).

with increasing adsorbent dosage, leading to an increased adsorption efficiency.

In order to investigate the effect of temperature on the adsorption efficiency, adsorption experiments were carried out at different temperatures (0, 20, 40, and 60 °C) (Fig. 6c). It could be found that the temperature had no remarkable effect on the removal efficiency, just accelerated the adsorption rate of SHC_{0.04}-500 toward MB. From the point view of energy saving, 20 °C was selected as the optimal temperature for adsorption over SHC_{0.04}-500. Based on the above results, it could be deduced that the adsorbent SHC_{0.04}-500 had a promising application at variable temperatures.

The adaptability of an adsorbent in a wide pH range is very important for the practical application of the adsorbent. Fig. 6d shows the influence of pH value on the removal performance of SHC_{0.04}-500 toward MB. The adsorption efficiency reached 15% when the pH value was 3. As the pH value continued to rise, the adsorption efficiency showed a remarkable increase, which achieved the highest efficiency at pH = 11. This result demonstrated the adaptability of SHC_{0.04}-500 under conditions close to neutral and alkaline

For investigating the applicability of SHC_{0.04}-500 to other dyes, adsorption experiments were carried out through selecting four different dyes as target pollutants (Fig. 6e). The cationic dyes MV and MG could be adsorbed over 85% to SHC_{0.04}-500. In contrast, the adsorbent showed very low adsorption efficiencies toward the anionic dyes OA and MO. Fig. 6f shows the zeta potential plots of $SHC_{0.04}$ -500 at different pH values.

Paper **Dalton Transactions**

When the pH value was 3, the surface of the adsorbent was positively charged, resulting in a lower adsorption efficiency toward MB. In contrast, when the pH value was increased from 3 to 11, the surface was negatively charged, leading to a higher adsorption efficiency toward MB. It was obvious that the adsorbent showed the excellent adsorption performance toward cationic dyes, thus it could be deduced that the electrostatic attraction was possibly the key factor in the adsorption process.

The adsorption efficiencies of SHC_{0.04}-500 toward various antibiotics with a concentration of 50 mg L⁻¹ were also examined (Fig. S2†). SHC_{0.04}-500 showed the highest adsorption efficiency toward NFO, which was close to 80% within 18 min. The results indicated that SHC_{0.04}-500 had great potential in removing antibiotics from wastewater.

The results of the cyclic adsorption experiments of MB over SHC_{0.04}-500 are shown in Fig. 7a. The adsorption efficiency decreased by only 5% after the first cycle, which still remained 78% after the fourth cycle. The decreased adsorption efficiency was probably related to the incomplete desorption and adsorbent loss. 50 After the adsorption of MB, the color of the adsorbent changed from yellow to dark green, and the dark blue MB turned to light blue, suggesting that MB was successfully adsorbed by SHC_{0.04}-500 (Fig. 7b).⁵¹

Fig. 7c demonstrates that the XRD pattern of SHC_{0.04}-500 basically remains unchanged after the adsorption. A new peak at 1327 cm⁻¹ emerged in the FT-IR spectra of SHC_{0.04}-500 after the adsorption, which was attributed to the C-C stretching vibrations of MB.52 Moreover, two spurious peaks at 1244 and 1490 cm⁻¹ related to the C-N stretching vibration of N-CH₃ in the MB structure were also detected in SHC_{0.04}-500 after adsorption, implying the successful adsorption of MB molecules on the surface of SHC_{0.04}-500.⁵³ Based on the above analysis, it could be concluded that SHC_{0.04}-500 exhibited excellent cycling and structural stability during the cycle tests.

Pseudo-first-order and pseudo-second-order models were employed to describe the adsorption process of SHC_{0.04}-500

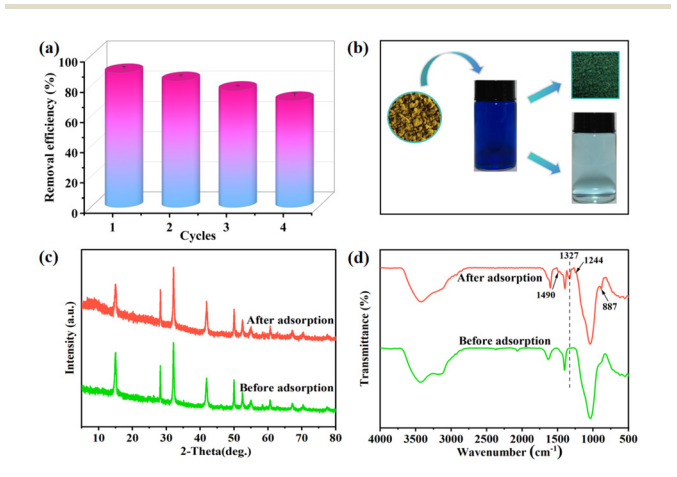


Fig. 7 The cycling performance of $SHC_{0.04}$ -500 (a). The color images of SHC_{0.04}-500 and MB (b). XRD patterns (c) and FT-IR spectra (d) of SHC_{0.04}-500 before and after adsorption.

toward MB. The pseudo-first-order and pseudo-second-order equations are presented as formulas (3) and (4), respectively:⁵⁴

$$\ln (q_e - q_t) = \ln q_e - k_1 t \tag{3}$$

$$\frac{t}{q_t} = \frac{1}{k_2 q_e^2} + \frac{1}{q_e} t \tag{4}$$

where q_t (mg g⁻¹) and q_e (mg g⁻¹) are the adsorption capacity of MB at time t and the equilibrium time, respectively. k_1 and k_2 are the related constants.

According to Fig. 8a, b, and Table S1,† the adsorption process of SHC_{0.04}-500 toward MB had both physical and chemical adsorption. The adsorption data matched well with the pseudo-first-order model ($R^2 = 0.99621$) than the pseudosecond-order model ($R^2 = 0.99325$), implying that the physical adsorption played a dominant role in MB adsorption over $SHC_{0.04}$ -500.

From the above Raman results, it could be seen that SHC_{0.04}-500 and HNTs(C)-500 had obvious G bands compared with HNTs, indicating that SHC_{0.04}-500 and HNTs(C)-500 contained a large number of aromatic structures with π electron clouds. Due to the conjugated π bond structure of MB, it was attracted to SHC_{0.04}-500 through π - π stacking, causing their electron clouds to overlap and resulting in chemical adsorption. The results showed that carbonized HNTs played a certain role in promoting chemical adsorption.

The adsorption isotherm models are proposed to explain the adsorption equilibrium and express the interactions between adsorbent and adsorbed molecules. 55 In this study, four adsorption models were used to analyze the adsorption data, including Langmuir, Temkin, Redlich-Peterson, and Freundlich models. The specific model expressions are shown in eqn (5)-(8), respectively.

$$\frac{C_{\rm e}}{q_{\rm e}} = \frac{1}{q_{\rm m}K_{\rm L}} + \frac{C_{\rm e}}{q_{\rm m}} \tag{5}$$

$$q_{\rm e} = A \ln \left(K_{\rm T} C_{\rm e} \right) \tag{6}$$

$$q_{\rm e} = \frac{K_{\rm p}C_{\rm e}}{1 + \alpha C_{\rm e}} \tag{7}$$

$$\ln q_{\rm e} = \ln K_{\rm F} + \frac{1}{n} \ln C_{\rm e} \tag{8}$$

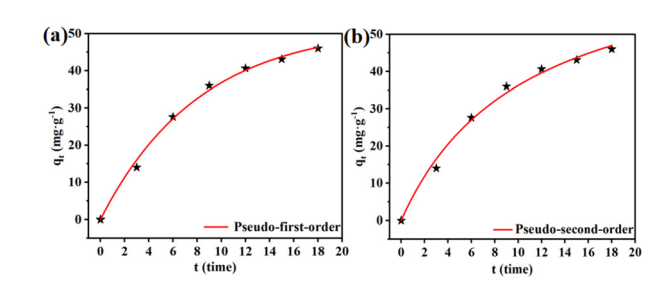


Fig. 8 The pseudo-first-order model (a) and the pseudo-second-order model (b) for MB adsorption over SHC_{0.04}-500.

where $C_{\rm e}$ (mg L⁻¹) and $q_{\rm e}$ (mg g⁻¹) are the concentration of MB in solution and the adsorbed amount of the adsorbent at adsorption equilibrium, respectively, and $q_{\rm m}$ (mg g⁻¹) is the maximum adsorbed amount of MB. $K_{\rm L}$, $K_{\rm T}$, $K_{\rm p}$, and $K_{\rm F}$ are the Temkin, Langmuir, Redlich–Peterson, and Freundlich model adsorption constants, respectively. A, α , and n are the constants of the Temkin, Redlich–Peterson, and Freundlich models, respectively.

Dalton Transactions

The fitting results of the four adsorption isotherm models are shown in Fig. 9 and Table S2.† The fitting coefficient of the Langmuir isotherm model ($R^2 = 0.96934$) was higher than those of the Freundlich ($R^2 = 0.91509$), Temkin ($R^2 = 0.95782$), and Redlich-Peterson ($R^2 = 0.96034$) isotherm models, suggesting that the Langmuir isotherm model could better describe the equilibrium data. The Langmuir model is based on the assumption of monolayer adsorption on the surface of a homogeneous adsorbent, where all adsorption sites are identical and there is no interaction between the adsorbed molecules. Therefore, the adsorption of MB over SHC_{0.04}-500 was monolayer adsorption.

As shown in Fig. S3,† HNTs(C)-500 exhibited a higher surface charge density than pristine HNTs, indicating that the carbon layer introduced the additional negative charges on the surface of HNTs(C)-500. In combination with the intrinsic charge properties of SnS₂, the electrostatic attraction toward the cationic dye MB was undoubtedly enhanced. Notably, at pH >3, all samples (HNTs, SnS₂, HNTs(C)-500, and SHC_{0.04}-500) have negative charges and SHC_{0.04}-500 exhibited the highest value. This enhancement was possibly related to the covalent bond formation between SnS₂ and HNTs(C)-500 during the composite synthesis, which induced electron redistribution and thus increased the overall negativity of SHC_{0.04}-500. Therefore, SHC_{0.04}-500 exhibited significantly higher adsorption efficiency toward cationic dyes than anionic dyes, which was consistent with the principle of opposite charge

Fig. 9 Langmuir (a), Temkin (b), Redlich–Peterson (c), and Freundlich (d) isothermal models for MB adsorption over $SHC_{0.04}$ -500.

attraction. The kinetic and isotherm models revealed that the adsorption process conformed to the typical physical adsorption. The zeta potential data confirmed a strong relationship between the enhanced surface negativity of $SHC_{0.04}$ -500 and its superior MB adsorption performance. It can be concluded that the electrostatic attraction dominated the adsorption process of MB over $SHC_{0.04}$ -500.

Fig. S4 and Table S3† show the pore size distribution curves, surface areas, and pore size distribution data of various samples, respectively. HNTs(C)-500 had a larger specific surface area than HNTs, which suggested that the carbon layer on HNTs was beneficial for increasing the specific surface area. SHC_{0.04}-500 had the largest specific surface area in comparison with those of HNTs, HNTs(C)-500, and SnS2. The larger specific surface area and smaller mesopores could provide more active sites, which was beneficial for enhancing the adsorption performance. The specific surface area and pore size of SHC_{0.04}-500 changed after MB adsorption (Fig. S5 and Table S3†), although the changes were not significant. This indicates that only a small portion of MB molecules had attached to the surface and filled the pores of SHC_{0.04}-500. Based on the above analysis, the large specific surface area and pore filling also contributed to the enhanced adsorption efficiency of SHC_{0.04}-500 toward MB.

Moreover, the results of FT-IR spectroscopy suggested that a new peak at 887 cm $^{-1}$ emerged in the FT-IR spectrum of HNTs (C)-500. This new peak was attributed to the C–H bond, which could provide active sites for adsorption. The peak intensity of SHC $_{0.04}$ -500 at 887 cm $^{-1}$ increased after MB adsorption, indicating that the C–H bending vibration was affected. Thus, it could be deduced that there was a π - π interaction between SHC $_{0.04}$ -500 and MB molecules, which was possibly another factor promoting the adsorption process. 57

In summary, there were four main factors contributing to the enhanced adsorption performance of SHC_{0.04}-500 toward MB, including electrostatic attraction, pore filling, large specific surface area, and π - π interactions (Fig. 10).



Fig. 10 The possible adsorption mechanisms of $SHC_{0.04}$ -500 toward

Conclusions

Paper

In this work, layered SnS2 was successfully anchored on the surface of EDTA-modified HNTs through a one-step hydrothermal method. The adsorbent SHC_{0.04}-500 was able to remove 90% of MB (50 mg L⁻¹) within 18 minutes, showing higher adsorption efficiency compared to those of SnS₂, HNTs, and HNTs(C)-500. The synthesized adsorbent could be applied in the treatment of various cationic dyes and antibiotics, and displayed wide adaptability in a temperature range of 0-60 °C and a pH range of 3-11. Kinetics fitting results indicated that MB adsorption over SHC_{0.04}-500 followed the pseudo-firstorder model, and the Langmuir model was found to be a better fit for describing the adsorption process. The mechanism investigation results suggested that electrostatic attraction, pore filling, large specific surface area, and π - π interactions contributed to the enhanced adsorption efficiency of $SHC_{0.04}$ -500.

Author contributions

Lan Yang designed and conducted the experimental studies, wrote the original manuscript, and conducted characterization studies. Qiyuan Lu gave some suggestions. Xiao Zhou made deep discussion. Tao Yang revised the manuscript. Chunfang Du supervised and commented on the manuscript.

Conflicts of interest

There are no conflicts to declare.

Data availability

The data that support the findings of this study are available from the corresponding author upon reasonable request.

Acknowledgements

This work was supported by the National Natural Science Foundation of China (52164024 and 52374258) and the Post-Subsidy Funds for the Inner Mongolia Key Laboratory of Chemistry and Physics of Rare Earth Materials (2021PT0003).

References

- S. M. Zhai, M. Li, D. Wang, L. Zhang, Y. Yang and S. Fu, J. Cleaner Prod., 2019, 220, 460–474.
- 2 H. Zhang, G. Xue, H. Chen and X. Li, *Chemosphere*, 2018, **191**, 64–71.
- 3 Y. Qi, M. Yang, W. Xu, S. He and Y. Men, *J. Colloid Interface Sci.*, 2017, **486**, 84–96.

- 4 M. Arshadi, F. Mousavinia, M. J. Amiri and A. R. Faraji, J. Colloid Interface Sci., 2016, 483, 118–131.
- 5 M. M. Mian, G. Liu and H. Zhou, *Sci. Total Environ.*, 2020, 744, 140862.
- 6 X. He, Y. Yang, Y. Li, J. Chen, S. Yang, R. Liu and Z. Xu, *Appl. Surf. Sci.*, 2022, **599**, 153898.
- 7 M. M. Vieira, A. S. P. Dornelas, T. D. Carlos, A. Pallini, C. Gravato, D. H. Pereira, R. A. Sarmento and G. S. Cavallini, *Chemosphere*, 2021, 283, 131117.
- 8 H. Khadivi, M. Sirousazar, V. Abbasi-Chianeh and E. Jalilnejad, *J. Polym. Environ.*, 2022, **30**, 3186–3202.
- 9 C. Lei, M. Pi, C. Jiang, B. Cheng and J. Yu, J. Colloid Interface Sci., 2017, 490, 242–251.
- 10 Y. Li, B. Xing, X. Wang, K. Wang, L. Zhu and S. Wang, Energy Fuels, 2019, 33, 12459–12468.
- 11 R. Zein, J. S. Purnomo, P. Ramadhani, Safni, M. F. Alif and C. N. Putri, *Arabian J. Chem.*, 2023, **16**, 104480.
- 12 B. Nissanka, N. Kottegoda and D. R. Jayasundara, *J. Mater. Sci.*, 2019, 55, 1996–2005.
- 13 M. J. Uddin, R. E. Ampiaw and W. Lee, *Chemosphere*, 2021, 284, 131314.
- 14 B. Farahani, M. Giahi, M. H. Ghorbani, R. Fazaeli and O. Moradi, *J. Nanostruct. Chem.*, 2023, 13, 303–320.
- 15 M. Massaro, R. Noto and S. Riela, *Molecules*, 2020, 25, 4863.
- 16 H. Zhang, Nanotechnol. Rev., 2017, 6, 573-581.
- 17 R. T. De Silva, R. K. Dissanayake, M. Mantilaka, W. Wijesinghe, S. S. Kaleel, T. N. Premachandra, L. Weerasinghe, G. A. J. Amaratunga and K. M. N. de Silva, ACS Appl. Mater. Interfaces, 2018, 10, 33913–33922.
- 18 Y. Song, P. Yuan, P. Du, L. Deng, Y. Wei, D. Liu, X. Zhong and J. Zhou, *Appl. Clay Sci.*, 2020, **186**, 105350.
- 19 Y. Zhang, F. Zhang, Z. Yang, H. Xue and D. D. Dionysiou, J. Catal., 2016, 344, 692–700.
- 20 H. Wei, C. Hou, Y. Zhang and Z. Nan, Sep. Purif. Technol., 2017, 189, 153–161.
- 21 S. Wang, B. Yang and Y. Liu, *J. Colloid Interface Sci.*, 2017, **507**, 225–233.
- 22 K. Kuśmierek, A. Świątkowski, E. Wierzbicka and I. Legocka, *Molecules*, 2024, **29**, 3099.
- 23 W. J. Liu, Y. Zhou, W. Gong, T. T. Tang, Y. Yang, C. Yao, S. X. Zuo and X. Z. Li, J. Appl. Chem. Biotechnol., 2025, 100, 625–634.
- 24 Y. Du and P. Zheng, Korean J. Chem. Eng., 2014, 31, 2051-2056.
- 25 W. S. Wang, H. Y. Xu, B. Li, L. Y. Dai, S. Q. Zhang, Y. Xu and S. Y. Qi, *Mater. Today Commun.*, 2023, 36, 106821.
- 26 R. Cheng, H. Li, Z. Liu and C. Du, *Minerals*, 2018, 8, 387.
- 27 H. Zhao, H. Fu, X. Yang, S. Xiong, D. Han and X. An, Int. J. Hydrogen Energy, 2022, 47, 8247–8260.
- 28 S. Mondal, S. Das and U. K. Gautam, *J. Colloid Interface Sci.*, 2021, **603**, 110–119.
- 29 S. Gedi, S. Alhammadi, J. Noh, V. R. M. Reddy, H. Park, A. M. Rabie, J. J. Shim, D. Kang and W. K. Kim, *Nanomaterials*, 2022, 12, 282.

- 30 L. Jin, Q. Sun, Q. Xu and Y. Xu, Bioresour. Technol., 2015, **197**, 348-355.
- 31 S. Lin, S. Li, Y. Zhang, T. Ma and H. Huang, J. Mater. Chem. A, 2021, 9, 17936-17944.
- 32 S. De Gisi, G. Lofrano, M. Grassi and M. Notarnicola, Sustainable Mater. Technol., 2016, 9, 10-40.
- 33 X. Bian, X. Lu, Y. Xue, C. Zhang, L. Kong and C. Wang, J. Colloid Interface Sci., 2013, 406, 37-43.
- 34 F. Duan, Y. Zhu, Y. Lu, J. Xu and A. Wang, J. Environ. Sci., 2023, 127, 855-865.
- 35 S. Sadjadi, Appl. Clay Sci., 2020, 189, 105537.

Dalton Transactions

- 36 D. Gu, W. Liu, J. Wang, J. Yu, J. Zhang, B. Huang, M. N. Rumyantseva and X. Li, Chemosensors, 2022, 10, 165.
- 37 T. Islam, M. R. Repon, T. Islam, Z. Sarwar and M. M. Rahman, Environ. Sci. Pollut. Res. Int., 2023, 30, 9207-9242.
- 38 W. Zhang, Y. Wang, W. Tao, H. Guan, C. Jiang, W. Tian and L. Hao, ACS Appl. Energy Mater., 2024, 7, 2504-2513.
- 39 Q. Le and Z. Cheng, Colloids Surf., A, 2022, 655, 130242.
- 40 M. Varga, T. Izak, V. Vretenar, H. Kozak, J. Holovsky, A. Artemenko, M. Hulman, V. Skakalova, D. S. Lee and A. Kromka, Carbon, 2017, 111, 54-61.
- 41 N. V. Chukanov, S. M. Aksenov and I. V. Pekov, Spectrochim. Acta, Part A, 2023, 287, 121993.
- 42 A. Saadati and S. Sheibani, Ceram. Int., 2022, 48, 30294-30306.
- 43 T. Ou, Y. Wu, W. Han, L. Kong, G. Song, D. Chen and M. Su, J. Hazard. Mater., 2022, 424, 127208.

- 44 M. Ismael, Chem. Phys. Lett., 2020, 739, 136992.
- 45 X. He, T. He, Y. Liu, Y. Zhou, B. Song, Y. Qi, L. Jiang, F. Liao and Z. Kang, Appl. Surf. Sci., 2022, 606, 154936.
- 46 Y. Liu, X. Yang, J. Ai, Q. Shang, D. Wang and G. Liao, Chem. Eng. J., 2023, 474, 145586.
- 47 F. Meng, J. Oin, H. Zhang, X. Xiong and R. Hu, Appl. Surf. Sci., 2023, 623, 157028.
- 48 M. S. Yilmaz, Microporous Mesoporous Mater., 2022, 330, 111570.
- 49 E. h. Yang and D. J. Moon, Top. Catal., 2017, 60, 697-
- 50 X. Zhang, R. Zhang, S. Niu, J. Zheng and C. Guo, J. Colloid Interface Sci., 2019, 554, 229-238.
- 51 L. Deng, P. Yuan, D. Liu, P. Du, J. Zhou, Y. Wei, Y. Song and Y. Liu, Appl. Clay Sci., 2019, 181, 105240.
- 52 Y. Li, B. Yu, Z. Hu and H. Wang, Chem. Eng. J., 2022, 429, 132105.
- 53 F. Chen, L. Ma, B. Li, P. Jiang, Z. Song and L. Huang, Nanomaterials, 2022, 12, 2352.
- 54 M. A. Rahman, D. Lamb, M. M. Rahman, M. M. Bahar, P. Sanderson, S. Abbasi, A. Bari and R. Naidu, J. Hazard. Mater., 2021, 409, 124488.
- 55 J. Villarroel-Rocha, D. Barrera, J. J. Arroyo-Gómez and K. Sapag, Adsorption, 2021, 27, 1081-1093.
- 56 R. Ezzati, Chem. Eng. J., 2020, 392, 123705.
- 57 O. V. Ovchinnikov, A. V. Evtukhova, T. S. Kondratenko, M. S. Smirnov, V. Y. Khokhlov and O. V. Erina, Vib. Spectrosc., 2016, 86, 181-189.